

# A Steerable Cross-axis Notched (SCAN) Continuum Manipulator

Yilin Cai, Xiaojie Ai, Anzhu Gao, *Member, IEEE*, and Weidong Chen, *Member, IEEE*

**Abstract**—This paper developed a Steerable Cross-axis Notched (SCAN) continuum manipulator based on Cylindrical Cross-axis Flexural Pivots (CCAFP). The design aims to address the trade-off between notched-tube compliant joints' range of motion and stiffness by integrating asymmetric cross-axis notch to the manipulator. Two pairs of cross-tiled beams are arranged at each joint section as the flexural member. The increased length of bending members and parallel flexures pairs could enlarge the range of motion within the constraint of ultimate strain and ensure the stiffness. The static model for single and multiple flexural joint sections is built to investigate the bending characteristic of the developed continuum manipulator. The Finite Element Analysis (FEA) is conducted to validate the static model and quantify the superiority of the proposed manipulator in bending angle and strain distribution compared with rectangular notched design. The model verification experiments and stiffness testing experiments are carried out to demonstrate that the developed continuum manipulator could bend to 172° by 7 N-acutance force.

## I. INTRODUCTION

Continuum manipulator provides a tremendous potential to operate within constrained environment in minimally invasive surgery (MIS) due to the compliance of the flexible backbone [1]–[3]. Within the various flexible backbones structures, notched-tube compliant mechanisms have increasingly been used in development of miniature dexterous continuum manipulators. These tendon-driven continuum manipulators are constructed by selectively etching away material from a tubular superelastic nitinol, thus featuring monolithic geometries and easy assembly. However, there exists a major trade-off between the range of motion and stiffness in the manipulator design, which must both be large enough for the manipulator to reach the required locations and exert the required tissue forces [1], [4].

Confined and unstructured spaces require large range of motion of a continuum manipulator for accessing hard-to-reach lumens, such as complex bronchial tree. Since the overall performance depends largely on the bending capability of one single section, much attention is paid to the notching patterns and the geometric design parameters on each section. The notching patterns used in bending joint design can be categorized as unidirectional asymmetric [4]–[7], bidirectional symmetric [8], [9], and bidirectional asymmetric [10]–[14], as shown in Figs. 1(a)–(c). In these joint designs, the manipulator either requires large force to

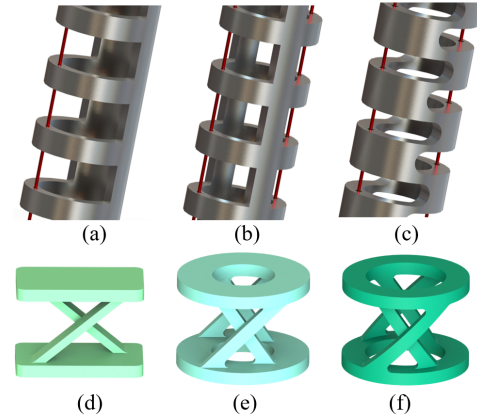


Fig. 1. Structure of different notched joints and flexural pivots. (a) Unidirectional asymmetric notch. (b) Bidirectional symmetric notch. (c) Bidirectional asymmetric notch. (d) Planar CAFP joint. (e) Integration of CAFP with cylinder tube. (f) CCAFP joint.

actuate or result in a high strain, e.g. it bends 80° using a force of 13 N [13] and bends 138.6° with a strain of 10.4% [5]. The limited strain profile caused by short or cornered flexure configuration after notching pose a challenge on increasing the range of motion. To improve the bending angle within the material's strain limit, Ryu *et al.* [15] proposed an active needle by adding fillets to the corners of the notch to reduce strain concentrations. Lobontiu *et al.* [16] proposed a general analytical compliance model for symmetric notch flexure hinges with circular corner-filled parabolic design. For these notched tubes, decreasing the joint's tube diameter and increasing the notch depth appear to have the most significant impact on the compact bending of individual notches, but they also significantly reduce stiffness especially when scaled below the 3 mm diameter range. Another intuitive approach to expand the workspace is to increase the number of bending sections while the long flexible backbone also leads to low stiffness [17].

Stiffness (directional bending, torsional, and axial) is critical for the manipulator to keep a stationary hold accuracy when completing a instrument positioning task and to carry appropriate weight end effector [7]. As Figs. 1(a)&(c) show, unidirectional and bidirectional asymmetric tubes are susceptible to transverse and axial forces due to the shifted neutral axis of the tube [18]. Eastwood *et al.* [4] presented a miniature notched manipulator integrated with the contact-aided compliant mechanism to increase the stiffness but it still resulted in a relative high stain of 5.81% (Nitinol). In another research of his [7], a unidirectional asymmetric joint could reach 0.125 mm/N stiffness by optimization design but it took up to 40 N tendon force to achieve a bending angle of 90°. Although it is related to the manipulator's

\*This work is supported by the Institute of Medical Robotics, Shanghai Jiao Tong University.

The authors are with the Institute of Medical Robotics and Department of Automation, Shanghai Jiao Tong University, and Key Laboratory of System Control and Information Processing, Ministry of Education, Shanghai 200240, China (Corresponding author: Weidong Chen, e-mail: wdchen@sjtu.edu.cn )

diameter, the higher driven force raised higher requirement for the safety of tendons against breakage, especially when considering the friction during transmission. Other studies managed to enhance the torsional, axial and payload stiffness by introducing twin-pivots [17], rolling contact [19], or constraining mechanism [20], respectively. These studies introduce either additional structure with higher manufacture difficulty or the friction. Therefore, this work aims to design a joint that is both large deformable with low actuation force and simultaneously stiff enough to manipulate tissue.

The Cross-Axis Flexural Pivot (CAFP)(see Fig. 1(d)) is made of two flexures that cross at an angle, often mid-length, between the grounded and output links [21], [22]. However, CAFP concept which is based on planar bending beams cannot meet the requirement of robotic MIS instruments like providing a steerable cylindrical shaft or central channels (see Fig. 1(e)). Based on CAFP, the cylindrical cross-axis flexural pivot (CCAFP) is proposed as an ultra-compact flexure. It has the benefit of being integrated into a hollow shaft without interfering with components internal to the shaft [21]. In this paper, we present a novel Steerable Cross-axis Notched (SCAN) continuum manipulator by introducing CCAFPA into the design of an asymmetric notched-tube compliant mechanism. The increased length of bending members and parallel flexures pairs in each joint could enlarge the range of motion within the constraint of ultimate strain and ensure stiffness. The main contribution is that we integrate the CCAFPA into a notched-tube compliant mechanism to solve the trade-off between the range of motion and stiffness, thus making the SCAN manipulator suitable for hard-to-reach lumen accessing and precise tissue manipulation.

The remainder of this paper is organized as follows: The structure design and manufacture process of the continuum manipulator is presented in Section II-A, followed by the static model in Section II B-C and the finite element validation and comparison in Section II D-E. The bending experiments are conducted to validate the model accuracy and the stiffness testing experiments are carried out in Section III. The discussion and conclusion are presented in Section IV.

## II. DESIGN AND MODELING

This section describes the design and manufacturing of the manipulator, the static model as well as the FEA validation and comparison.

### A. Design and Manufacture

When we dismiss the variety of the material's strain limits, both of the range of motion and stiffness attributes are primarily a function of a manipulator's structural design—in particular, its backbone cross-sectional geometry [1]. During bending, strain is proportional to distance from the neutral axis of the backbone cross section, which is determined by the geometric features bending flexural member of each section. Focusing on each notched section, we create a longer bending beam with non-uniform cross-section which serves as the flexural member by introducing CCAFPA . Thus, in

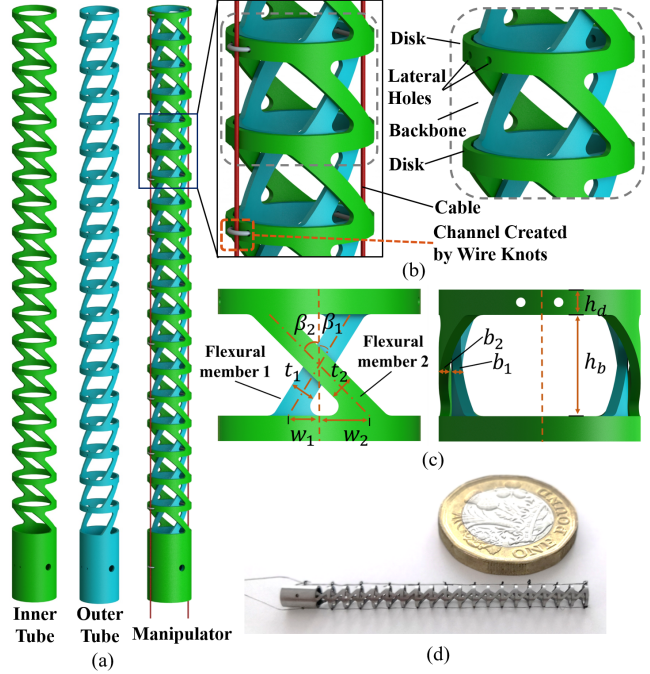


Fig. 2. Structure of proposed continuum manipulator. (a) Models of inner tube, outer tube and the assembled manipulator. (b) Cable routing channels created by knots of Nitinol wires, which pass through the lateral holes on the disks. (c) Single section of the flexural joints taking use of a CCAFPA. (d) Prototype of the manipulator.

contrast to traditional design where compliant beams perpendicular to adjacent disks are flexural members (rectangular notch), the higher second area of inertia and longer beam length would result in smaller strain or larger bending angles. Moreover, considering the stability and overall stiffness of the manipulator, two beams are arranged in two opposite tilting directions to form a cross-axis flexure.

As shown in Fig. 2(a), the manipulator arranged the flexures at the outer wall of the two aligned tube shafts with notched patterns micromachined along the length. Such nested tubes can ensure the clearance that prevents the two crossing beams colliding with each other during the bending process. It enable easier notching of the symmetrical or asymmetrical patterns especially even when there is an overlap of the cross-beams, which reduces the manufacturing difficulty. Each tube consists of 19 sections and each section includes a backbone and a disk (see Fig. 2(b)). The backbone is the bending part of the section which has two parallel flexural member pairs in both sides of the tube. The flexural members are actually two elliptical beams with variable cross sections (see Fig. 2(c)). The specifications of the manipulator including tube and flexural member dimensions are summarized in Table I. The total length of the manipulator is 43 mm including a 5-mm robot base.

The proposed continuum manipulator is driven by cables while the clearance between the two tubes and thin thickness of each tube proposed difficulty in creating the cable channels within the manipulator body. We create the channels by routing a Nitinol wire through the lateral holes pre-machined on the disk and then tying it into a knot (see Fig. 2(b)). The nitinol wire is 0.1mm in diameter with good superelasticity,

which makes the channel strong enough to bear and transmit the cable tension applied to the manipulator. By routing through the lateral holes, the disks on the inner and outer tube are strictly aligned, leaving the relative motion only to the flexural members. The lateral holes are machined every other disk to reduce assembly difficulties.

The manipulator is manufactured and assembled as shown in Fig. 2(d). The outer and inner tubes are made of superelastic nitinol for high bending capability on which the notch patterns are fabricated using femtosecond laser cutting (LUMENOUS PEIERTECH Ltd., Jiangyin, China). The 0.1 mm-diameter wires made of stainless steel are used as driven cables for their high Young's modulus and small elongation at high tension. This proposed SCAN continuum manipulator has the following advantages: (1) It is a monolithic structure capable of withstanding high axial forces as well as forces in the plane transverse to the bending plane. (2) It has the ability to selectively alter the stiffness and range of motion by changing the crossing angle of the flexural members. (3) It will result in smaller strain in the flexural member to improve the safety of the manipulator, which in turn enable larger deflection within the constraint of the material's ultimate strain.

### B. Static Model: Single Section

The modeling of single-section static model starts from analysis a planar CAFP. Different from most flexible joints obeying the assumption that the bending shape of a flexible joint is a standard arc, the joint deflection of the proposed manipulator is naturally decided by the combined behaviour of the two flexural members. The Beam-Constraint Model (BCM), a closed-form method capable of capturing nonlinearities of a flexible beams in their intermediate deflection range (i.e. 10% – 15% of the length), has been well used for modeling of the CAFP [23]–[25].

Fig. 3(a) shows a simple beam subject to transverse force  $F$ , axial force  $P$ , and moment  $M$  at its free end, resulting in axial and transverse deflections  $\delta x$  and  $\delta y$  and end slope  $\alpha$ .  $I$  represents the area moment of inertia of the beam cross section. BCM models the load-deflection relations of the

TABLE I  
SPECIFICATIONS OF THE PROPOSED CONTINUUM  
MANIPULATOR

| Symbol      | Description  | Outer tube | Inner tube |
|-------------|--|------------|------------|
| $i$         | Index of the flexural member                             | 1          | 2          |
| $n$         | Number of sections                                       | 19         | 19         |
| $\Phi_{od}$ | Outer diameter of the notched tube [mm]                  | 3.2        | 2.8        |
| $\Phi_{id}$ | Inner diameter of the notched tube [mm]                  | 2.9        | 2.5        |
| $\beta_i$   | Tilting angle of the flexural member [ $^\circ$ ]        | 31.9       | 45.0       |
| $L_i$       | Length of each flexural member [mm]                      | 1.89       | 2.26       |
| $w_i$       | Distance of flexural member end to the central axis [mm] | 0.50       | 0.80       |
| $t_i$       | In plane thickness of the member [mm]                    | 0.4        | 0.4        |
| $d_i$       | Radial thickness of each backbone [mm]                   | 0.15       | 0.15       |
| $h_b$       | Height of each backbone [mm]                             | 1.6        | 1.6        |
| $h_d$       | Height of each disk [mm]                                 | 0.4        | 0.4        |

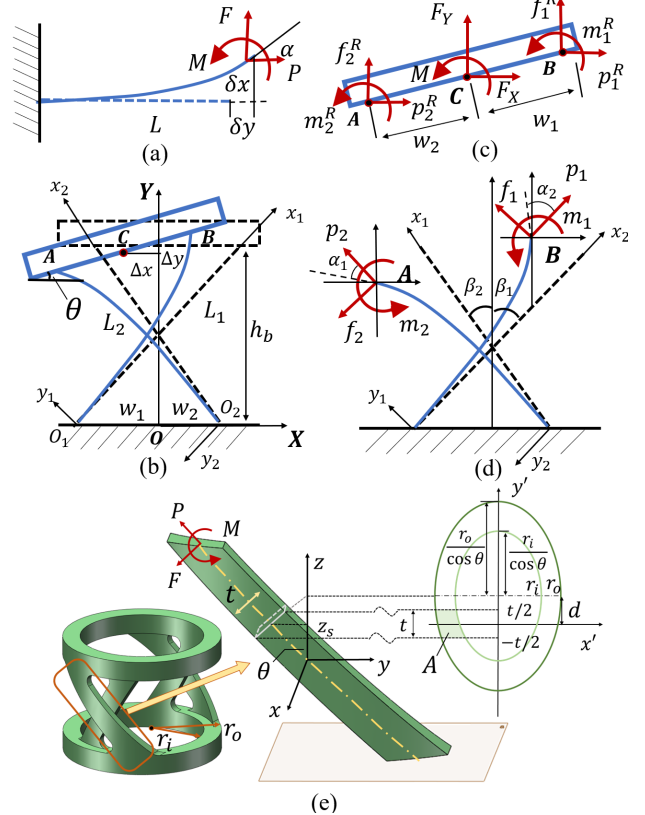


Fig. 3. Static model schematic of one single section. (a) Deflection of a simple beam subject to external load  $F, P$  and  $M$  applied at its free end. (b) The geometrical profile and global displacement of a planar CAFP. (cd) Free-body-diagram of the CAFP under the global load. (e) The cross section (shaded area  $A$ ) of an elliptical flexural member.

beam using the parametric equations as Eqs. (1)&(2).

$$\begin{bmatrix} f_i \\ m_i \end{bmatrix} = G_c \begin{bmatrix} \delta y_i \\ \alpha_i \end{bmatrix} + p_i P_c \begin{bmatrix} \delta y_i \\ \alpha_i \end{bmatrix} + p_i^2 Q_c \begin{bmatrix} \delta y_i \\ \alpha_i \end{bmatrix} \quad (1)$$

$$\delta x_i = \frac{t_i^2 p_i}{12 L_i^2} - \frac{1}{2} \begin{bmatrix} \delta y_i \\ \alpha_i \end{bmatrix}^T U_c \begin{bmatrix} \delta y_i \\ \alpha_i \end{bmatrix} - p_1 \begin{bmatrix} \delta y_i \\ \alpha_i \end{bmatrix}^T V_c \begin{bmatrix} \delta y_i \\ \alpha_i \end{bmatrix} \quad (2)$$

where the load parameters  $f_i, p_i, m_i$  and the deflection parameters  $\delta x_i, \delta y_i$  are normalized with respect to the beam parameters in Eq.(3). The coefficient is given in Eq.(4).

$$m_i = \frac{M_i L_i}{EI_i}, f_i = \frac{FL_i^2}{EI_i}, p_i = \frac{PL_i^2}{EI_i}, \delta x_i = \frac{\Delta x_i}{L_i}, \delta y_i = \frac{\Delta y_i}{L_i} \quad (3)$$

$$G_c = \begin{bmatrix} 12 & -6 \\ -6 & 4 \end{bmatrix}, P_c = U_c = \begin{bmatrix} 6/5 & -1/10 \\ -1/10 & 2/15 \end{bmatrix}, Q_c = V_c = \begin{bmatrix} -1/700 & 1/1400 \\ 1/1400 & -11/6300 \end{bmatrix} \quad (4)$$

The bottom and output links of the CAFP are assumed to be rigid bodies and Fig. 3(b) demonstrates the deformed joint under the external load  $M, F_x, F_y$  applied to the center of the output link (point C). Eqs.(5) & (6) gives the global

statics equilibrium of each joint.

$$M = (w_1 + w_2) \frac{EI_2}{L_2^2} [\sin \theta - \cos \theta] \begin{bmatrix} \sin \beta_2 & \cos \beta_2 \\ -\cos \beta_2 & \sin \beta_2 \end{bmatrix} \begin{bmatrix} p_2 \\ f_2 \end{bmatrix} + w_1 [\sin \theta - \cos \theta] \begin{bmatrix} F_x \\ F_y \end{bmatrix} + \frac{EI_1}{L_1} m_1 - \frac{EI_2}{L_2} m_2 \quad (5)$$

$$\begin{bmatrix} F_x \\ F_y \end{bmatrix} = \frac{EI_1}{L_1^2} \begin{bmatrix} -\sin \beta_1 & \cos \beta_1 \\ -\cos \beta_1 & -\sin \beta_1 \end{bmatrix} \begin{bmatrix} p_1 \\ f_1 \end{bmatrix} + \frac{EI_2}{L_2^2} \begin{bmatrix} \sin \beta_2 & \cos \beta_2 \\ -\cos \beta_2 & \sin \beta_2 \end{bmatrix} \begin{bmatrix} p_2 \\ f_2 \end{bmatrix} \quad (6)$$

The CCAF used in our manipulator is asymmetric so the angle  $\beta_{1,2}$  and the beam end distance  $w_{1,2}$  with the central axis are unequal. Fig. 3(c) demonstrate the reaction force between the output link and the flexural members. Then, what we concern is the global displacements  $\Delta x, \Delta y$  and the bending angle  $\theta$ , which is given by the global geometric constraint equations as Eqs.(7) & (8).

$$\theta = \alpha_1 = \alpha_2 \quad (7)$$

$$\begin{bmatrix} (w_1 + w_2) + (w_2 + w_1) \cos \theta \\ (w_1 + w_2) \sin \theta \end{bmatrix} = \begin{bmatrix} \sin \beta_2 & \cos \beta_2 \\ -\cos \beta_2 & \sin \beta_2 \end{bmatrix} \begin{bmatrix} x_A \\ y_A \end{bmatrix} + \begin{bmatrix} \sin \beta_1 & -\cos \beta_1 \\ \cos \beta_1 & \sin \beta_1 \end{bmatrix} \begin{bmatrix} x_B \\ y_B \end{bmatrix} \quad (8)$$

where  $[x_A \ y_A]^T$  and  $[x_B \ y_B]^T$  is the end position of each deformed beam with respect to the coordinate system  $O_2x_2y_2$  and  $O_1x_1y_1$  placed at the fixed end (see Fig. 3(b)).

$$\begin{bmatrix} x_A \\ y_A \end{bmatrix} = \begin{bmatrix} L_2(1 + \delta_{x2}) \\ L_2\delta_{y2} \end{bmatrix}, \begin{bmatrix} x_B \\ y_B \end{bmatrix} = \begin{bmatrix} L_1(1 + \delta_{x1}) \\ L_1\delta_{y1} \end{bmatrix} \quad (9)$$

Therefore, we can get the displacement and the bending angle of the output link with respect to the coordinate systems  $OXY$  placed at the center of the bottom link by solving above equations.

$$\begin{bmatrix} \Delta x \\ \Delta y \end{bmatrix} = \begin{bmatrix} -\sin \beta_2 & -\cos \beta_2 \\ \cos \beta_2 & -\sin \beta_2 \end{bmatrix} \begin{bmatrix} x_A \\ y_A \end{bmatrix} + \begin{bmatrix} w_2 + w_2 \cos \theta \\ w_2 \sin \theta \end{bmatrix} - \begin{bmatrix} 0 \\ L_2 \cos \beta_2 \end{bmatrix} \quad (10)$$

Since the CCAF contains two parallel couples of cross-beams, the final displacement of a CCAF joint under the load  $F_x, F_y, M$  would be half of the results given by Eqs.(7) & (10) which are solve for single planar CAFP specifically. Another major difference between CCAF and CAFP is the elliptical flexures with variable cross sections (see Fig. 3(e)). The cross section of the flexural member formed by notching a cylinder with a outer diameter  $r_o$  and inner diameter  $r_i$  lies on the surface enclosed by the two ellipses (see the shaded area  $A$  in Fig. 3(e)). The two ellipses are described by major semiaxis  $r_o, r_i$ , minor semiaxis  $r_o/\cos(\theta), r_i/\cos(\theta)$  and the center offset  $d$ . Creating a coordinate system at the beam center, we will have the  $d = z_s \sin \theta / \cos^2 \theta$  ( $-h_b/2 < z_s <$

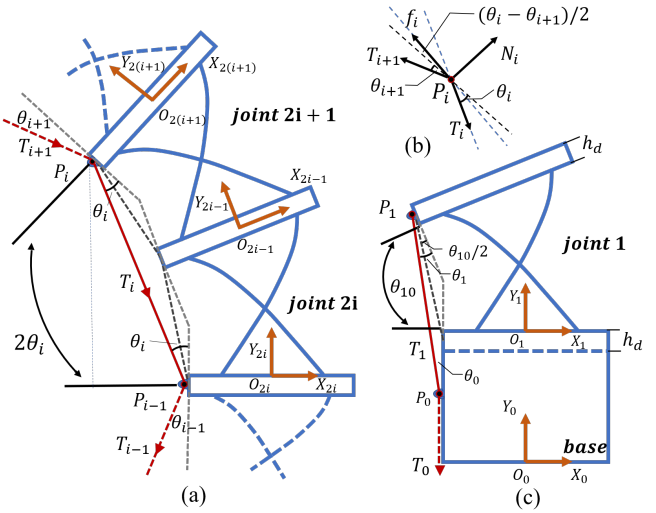


Fig. 4. Static model schematic of multiple sections coupled with cable tension. (a) Segment  $i$  including joint  $2i$  and joint  $2i+1$  subject to the cable tension  $T_i$ . (b) Free-body-diagram of cable  $a$  at the routing knot point  $P_i$ . (c) Segment 1 including joint  $i$  and the manipulator base subject to  $T_1$  and the input tension  $T_0$ .

$h_b/2$ ). Thus the area moment of inertia along the central axis of CCAF is given in Eq.(11).

$$I(z_s) = \int_A y'^2 dA = \int_{-t/2}^{t/2} y'^2 (\sqrt{r_o^2 - (y' \cos \theta - z_s \tan \theta)^2} - \sqrt{r_i^2 - (y' \cos \theta - z_s \tan \theta)^2}) dy' \quad (11)$$

For planar CAFP, the bending beam has rectangular cross section and constant area moment of inertia  $I = t^3 b / 12$ . It can be estimated that the area moment of inertia of such elliptical flexural member is a little greater than the rectangular one, resulting difference of the CCAF and the CAFP with same geometric specifications. To simplify the solving process, the numerical average value of  $I(z_s)$  along the member is calculated as constant equivalent inertia  $I_{e1}$  and  $I_{e2}$  in substitute of  $I_1$  and  $I_2$  in the modeling of planar CAFP. The equivalence would result in acceptable error as described in Section II-D. Consequently, the deflection of a single section in our manipulator under external load could be derived by solving the Eqs.(1)-(10).

### C. Static Model: Multiple Sections

The continuum manipulator is driven by cable while the cable is routed through every other disk. Here the two joints  $2i$  and  $2i+1$  ( $i = 1 \dots \frac{n+1}{2}$ ) between two adjacent routing knots that are driven by the same subsection of the cable are taken as a segment  $i$ , while the first joint along with the manipulator base is segment 1. Figs. 4 (a)&(c) show the free-body diagram of the segment. The bending angles of the two joints in the same segment are assumed to be the same as  $\theta_i$ . In multiple sections static model, to propagate the cable tension of the  $i$ -th section to the upward or backward one, the statics equilibrium of cable at point  $P_i$  (see Fig. 4(b)) is expressed as

$$T_{i+1} \cos\left(\frac{\theta_i + \theta_{i+1}}{2}\right) + f_i - T_i \cos\left(\frac{\theta_i + \theta_{i+1}}{2}\right) = 0 \quad (12)$$

$$T_{i+1} \sin\left(\frac{\theta_i + \theta_{i+1}}{2}\right) + T_i \sin\left(\frac{\theta_i + \theta_{i+1}}{2}\right) - N_i = 0 \quad (13)$$

where  $T_{i+1}$  and  $T_i$  are the cable tensions shown in Fig. 4;  $f_i$  and  $N_i$  are the friction and normal force at  $\mathbf{P}_i$ . Here the friction force is modeled as  $f_i = \mu_i \cdot N_i$  where  $\mu_i = \eta_i \cdot \mu_{s,k}$  is the friction coefficient with its direction. As previously built [10], [26],  $\eta_i$  is adjustable coefficient at the interaction point and  $\mu_{s,k}$  is static or kinetic friction coefficient. Here, only forward sliding status  $\eta_i$  is considered so  $\eta_i = 1$ .

Then the cable tension will propagate from the base to the tip as the input force is  $T_0$ . The attenuation of the tension in the adjacent segments is expressed as

$$T_{i+1} = T_i \cdot \frac{\cos\left(\frac{\theta_i + \theta_{i+1}}{2}\right) - \mu_i \sin\left(\frac{\theta_i + \theta_{i+1}}{2}\right)}{\cos\left(\frac{\theta_i + \theta_{i+1}}{2}\right) + \mu_i \sin\left(\frac{\theta_i + \theta_{i+1}}{2}\right)}, i = 1 \dots \frac{n+1}{2} \quad (14)$$

$$T_1 = T_0 \cdot \frac{\cos(\theta_0/2) - \mu_i \sin(\theta_0/2)}{\cos(\theta_0/2) + \mu_i \sin(\theta_0/2)} \quad (15)$$

where  $\theta_0$  is the angle between  $T_1$  and  $T_0$  as show in Fig. 4(c). Here we have  $\theta_1 = \theta_{10} - \theta_0$  and  $\theta_{10}$  is the actual bending angle of the first joint. The relationship between  $\theta_0$  and  $\theta_{10}$  is given as

$$\theta_0 = \tan^{-1} \left( \frac{-x_{P1}(\theta_{10}) - r_d}{y_{P1}(\theta_{10}) + \frac{3}{2}h_d + h_b} \right) \quad (16)$$

where  $[x_{P1}(\theta_{10}) \ y_{P1}(\theta_{10})]$  is the position of  $\mathbf{P}_1$  with respect the coordinate  $O_1X_1Y_1$ . Once the cable tension is given, the external load can be derived from Eq.(17).

$$F_{xi} = T_i \sin(\theta_i/2), F_{yi} = -T_i \cos(\theta_i/2), M_i = r_i T_i \cos(\theta_i/2) \quad (17)$$

We can derive the bending angles of all the  $n$  flexible joints using the single section model developed in Section II-B. We define the shape of the continuum manipulator as a series of discrete points at its joints' centers (i.e. the center of the upper surface of the disk). The transformation matrix from the frame at  $\{O_i\}$  to the frame at  $\{O_{i+1}\}$  is expressed as follows:

$$\mathbf{A}_i^{i+1} = \begin{bmatrix} 1 & 0 & 0 & 0 \\ 0 & \cos \theta_i & -\sin \theta_i & \Delta x_i \\ 0 & \sin \theta_i & \cos \theta_i & \Delta y_i \\ 0 & 0 & 0 & 1 \end{bmatrix} \quad (18)$$

Their absolute positions defined at the global frame are defined by Eq.(19)

$$\mathbf{A}_G^{tip} = \mathbf{A}_0 \prod_{i=1}^n \mathbf{A}_i^{i+1} \mathbf{A}_d \quad (19)$$

$$\mathbf{A}_0 = \begin{bmatrix} \mathbf{I}_{3 \times 3} & [0 \ 0 \ h_0]^T \\ 0 & 1 \end{bmatrix}, \mathbf{A}_d = \begin{bmatrix} \mathbf{I}_{3 \times 3} & [0 \ 0 \ h_d]^T \\ 0 & 1 \end{bmatrix} \quad (20)$$

where  $\mathbf{A}_0$  is the transformation matrix from the global frame  $\{O_0\}$  to the first joint's frame  $\{O_1\}$ ,  $\mathbf{A}_d$  denotes the translation along the disk.

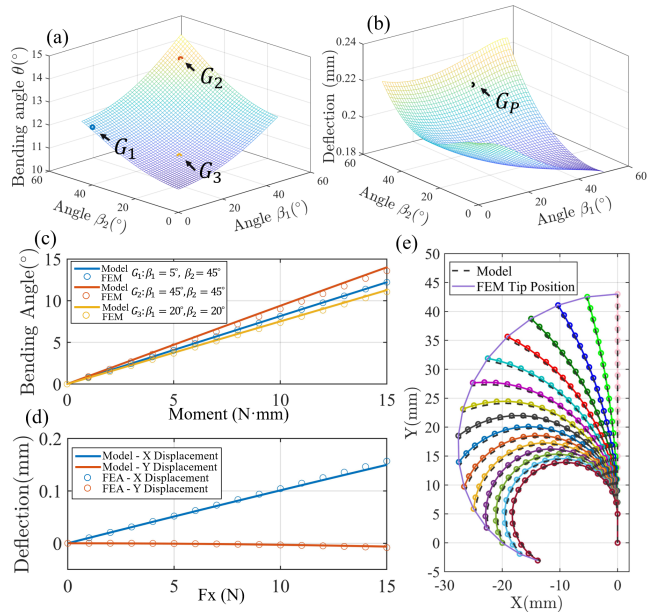


Fig. 5. Model analysis and FEA validation. (a) Estimation of a single joint bending with crossing angles under the pure external moment of 15 N-mm. (b) Estimation of a single joint deflection with different with crossing angles under a 10 N-lateral force. (c) Comparison of the model and FEA of three angle profiles  $[G_1 \ G_2 \ G_3]$ . (d) Comparison of the model and FEA of the joint deflection under a lateral force  $F_x$ . (e) Comparison of the model and FEA of the entire manipulator under pure moment.

#### D. Model Analysis and FEA Validation

The crossing angle between each flexural member and the central axis significantly affects the stiffness (i.e. bending and deflection under specific load) of the manipulator. According to the static model, it is fond that under pure moment larger crossing angle results in larger bending angle of a single joint. However, under the application of lateral force, the crossing notch has the potential to decrease the deflection which means a higher transverse stiffness (see Fig. 5(b)). As we have not chosen the optimal parameters, the proposed manipulator (whose geometric profile is  $G_P$  in Fig. 5(b)) would result in a little larger deflection compared with the non-crossing notch based design.

Finite Element Analysis (FEA) is then used to validate the proposed static model in ABAQUS 2016. Three angle profiles  $[G_1 \ G_2 \ G_3]$  are selected in comparison with the FEA results as shown in Fig. 5(c). The theoretical model fits the FEA result well, leaving mean errors for the three angle profiles as  $[0.16\% \ 2.01\% \ 0.76\%]$ . Meanwhile, the angle profile  $G_P$  is used for joint deflection comparison under a 10 N-lateral force (see Fig. 5(d)). The results obtained by both methods are in good consistent that the max error is 0.0071 mm in X-direction and 0.0019 mm in Y-direction. The multi-sectional static model of the entire manipulator is also compared with the FEA results as Fig. 5(e) shows. A pure moment of 15 N-mm is applied to the manipulator tip in 15 average steps. Both the manipulator shape and the tip position reached a good agreement with a mean tip position error of 0.53 mm, 1.24% of the manipulator length.

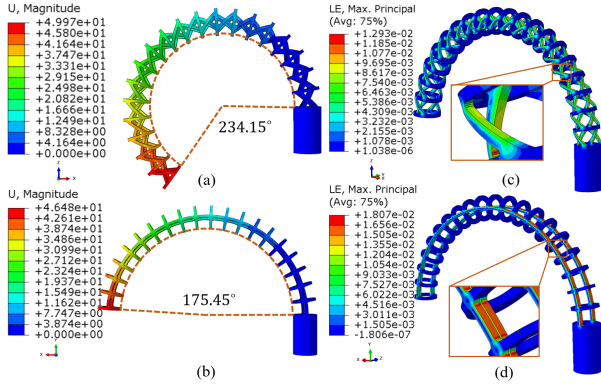


Fig. 6. FEA result comparison of our manipulator with traditional design.(ab) Bending angle of our manipulator and the traditional one. (cd) Strain distribution of our manipulator and the traditional one at the same bending angle of about 175°.

#### E. FEA Results Comparison

Bending performance and the strain distribution of the two types of notched continuum manipulator is simulated and compared by FEA in this subsection to illustrate the superiority of the proposed manipulator. Traditional bidirectional symmetric notched manipulator whose flexural member is a straight beam is modeled with the same geometric profile as our proposed SCAN manipulator(e.g. same backbone height, inner and outer diameter and joint numbers). As is shown in Figs. 6(a)&(b), the two types of manipulator are bent under the same external 9 N·mm pure moment applied to the tip center, while the bending angle of our manipulator is 58.7° larger than the traditional one. It indicates a 33.5% improvement in the range of motion.

When applying a 7.35 N-mm-moment to the SCAN manipulator, the bending angle reaches 175.90° which is similar to that of the traditional one under 9 N-mm moment. Therefore, to reach the same bending angle, the SCAN manipulator requires 22.45% less force to actuate. Figs. 6(c)&(d) demonstrate the stain distribution at the same bending angle where the max strain of our manipulator is 1.293% in contrast to 1.807% of the traditional one. Although the peak strain concentrates at corner of the elliptical beam on our manipulator, the stain is unevenly distributed and much smaller than that of the straight beam. To avoid permanent deformation, the design peak strain of Nitinol is usually defined as less than 5% resulting in a safety factor of 1.6 based on the manufacturer recommended value of 8% [27]. It is concluded that our proposed manipulator could work safely within the constraint of ultimate strain and also introduces 28.4% smaller strain than the traditional design.

### III. EXPERIMENTS AND RESULTS

To evaluate the static model and make a more in-depth stiffness analysis of the proposed continuum manipulator, the free bending and stiffness testing experiments are conducted.

#### A. Experimental Setup

A continuum manipulator prototype was constructed and fixed on a platform, shown in Figs. 7(a)&(c). The driven cables was guided by pulleys and its distal end was fixed on

the winding link connected with the motor output shaft. The servo motors (MX-28R, Dynamixel, Robotis, South Korea; 0.088° resolution) were used to actuate the manipulators by pulling or releasing the cables. The load cells (AT8300, Auyoda, China) were integrated to the pulleys to measure the cable tension, which transforms the tension to the compression force to the load cell by a 120° intersection angle (see Fig. 7(b)). The cable tension can be recorded in real time by a force display. A XYZ-Axis linear stage (Huike, Shenzhen, China) was used to applied the external force applied to the manipulator tip. A CMOS camera (UC30, MOKOSE, China) was mounted over the manipulator to capture the shapes of manipulator during deformation.

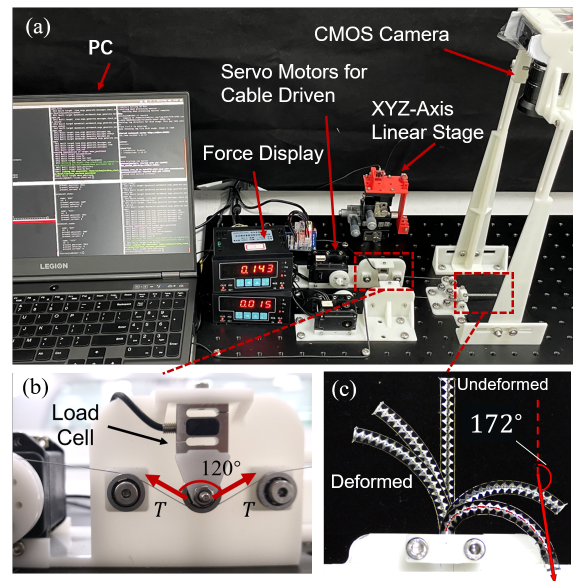


Fig. 7. Experimental setup.(a) Overview of the experiment platform. (b) Cable tension sensor integrated with a load cell. (c) The continuum manipulator prototype in the case of deformation and non-deformation.

#### B. Free Bending Experiment

The tendon was actuated from 0 to 4 N in 0.5 N increment and then released to 0 N in 0.5 N decrement. Three groups of data were obtained by repeating this process for three times which is also used for calibration. Here, the calibration process is to identify the Young's modulus and the friction coefficient which can be treated as an constrained optimization problem. The sequential quadratic programming method was used to find a minimum of total tip errors between experimental results and model results. The problem is defined as minimizing the constrained nonlinear multivariable function by using *fmincon* in MATLAB R2020a.

The bending images of the manipulator from 1-4 N are shown in Fig. 8(a). The calibrated friction coefficient and Young's modulus are 0.08 and 67 GPa, respectively. Fig. 8 demonstrates the model estimation results and the experimental results. The mean tip error is  $0.41 \pm 0.24$  mm and its normalization with the total flexible length of the manipulator (38 mm) is  $1.074\% \pm 0.064\%$ . The max bending angle could reach 172° with cable tension about 7 N (see Fig. 7(c)).

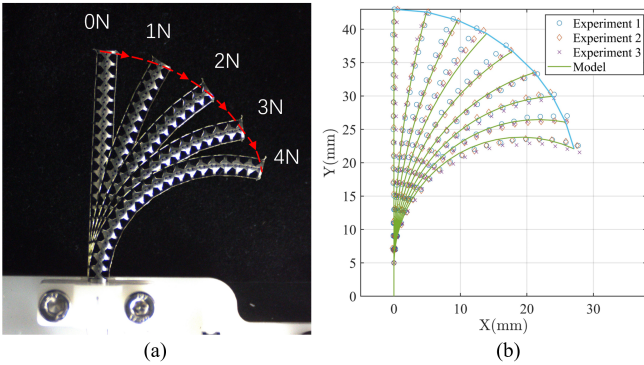


Fig. 8. Experimental and model results of manipulator bending. (a) Images of manipulator prototype bending from 1-4N. (b) Comparison of experimental and model results.

### C. Stiffness Testing Experiment

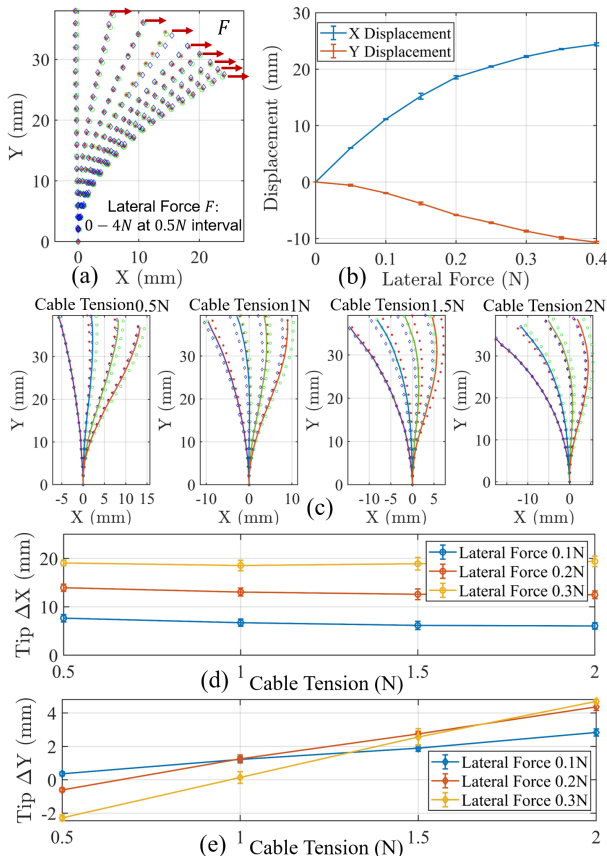


Fig. 9. Stiffness testing of the manipulator under lateral force. (ab) Manipulator shape deflection and tip displacement under 0-0.4N lateral force without cable tension. (cde) Manipulator shape deflection and tip displacement under 0-0.3N later force combined with 0-2N cable tension.

Experiments were conducted by applying a lateral force to the manipulator tip to analyze the deflection under external load, which directly reflect the stiffness of the manipulator. As is shown in Figs. 9(a)&(b), the manipulator without cable tension deflected under the lateral force from 0.1 N to 0.4 N at 0.05 N increment, resulting in 26.61 mm tip displacement at 0.4 N. As what can be found in Fig. 9(c),(d)&(e), cable tension would not result in significant change in X displacement of manipulator tip under the lateral

load. When later force is 0.3 N, the tip displacement is 19.95 mm with 2N cable tension in contrast to 23.87 mm without cable tension. Here we defined the free lateral stiffness as the tip displacement divided by lateral force which is 66.53 mm/N. However, the manipulator's overall stiffness also depends largely on the diameter, total length and the geometric parameters of notch pattern. Evaluation of the performance this cross-axis notch in comparison with other reported designs is given later in discussion.

## IV. DISCUSSION AND CONCLUSION

In this paper, we presented a novel Steerable Cross-axis Notched (SCAN) continuum manipulator by introducing the use of Cross-axis Flexural Pivot. It enables large range of motion within the constraint of the material's ultimate strain by notching a cross-tilted bending member of the flexural joint. Static models of single and multiple sections were developed which accurately described the bending behavior of the manipulator. The SCAN manipulator was compared to a manipulator of equivalent size but used traditional symmetric rectangular notch by FEA. The bending angle has a 33.5% improvement under the same driven force with a better stain distribution. The experiment indicates that the SCAN manipulator could reach 172° using only 7 N actuation force, in contrast to 80°—13 N as reported in [10] which also uses Nitinol. Since the range of motion is also affected significantly by the manipulator's overall dimensions, we use the average curvature of one single notched section under unit actuation force to evaluate the bending performance. This value is calculated as 0.67 of our manipulator in contrast to 0.18 of the manipulator in [10] and 0.08 in [13]. The higher value indicate the ability to achieve a lager range of motion of the notched tube evening using a lower force. Considering the safety of manipulator driven cables and the force loss during transmission, this characteristic is critical in medical instrument design. Due to the non-constant curvature bending caused by friction, the performance of our manipulator could even be better.

Analysis on single section statics has revealed that this cross-axis design could reduce the deflection under lateral force. The free lateral stiffness is also related to the manipulator's overall size. We use the length normalized stiffness as a evaluating indicator whose value is calculated as 1.75 of our manipulator, compared to 2.04 of the notched tube and 1.28 of a contact-aided tube both developed in [4]. This analysis does not consider how the cross-notched tubes compares to other notch design that is specifically optimized for stiffness or range of motion. However, the model proposed serves as a design guideline to understand how variations in cross-notching topology can be utilized to attain the desired motion while mitigate stiffness loss. In the future, we will work towards the task-oriented optimization design to maximize the superiority of this cross-axis notched manipulator. In addition, other structure modification can be integrated with the cross-axis notch like contact-aided block. A more elegant cable routing method could also help us decrease the model error.

## REFERENCES

- [1] J. Burgner-Kahrs, D. C. Rucker, and H. Choset, "Continuum robots for medical applications: A survey," *IEEE Transactions on Robotics*, vol. 31, no. 6, pp. 1261–1280, 2015.
- [2] T. da Veiga, J. H. Chandler, P. Lloyd, G. Pittiglio, N. J. Wilkinson, A. K. Hoshier, R. A. Harris, and P. Valdastri, "Challenges of continuum robots in clinical context: A review," *Progress in Biomedical Engineering*, vol. 2, no. 3, p. 032003, 2020.
- [3] M. Jha and N. R. Chauhan, "A review on snake-like continuum robots for medical surgeries," in *IOP Conference Series: Materials Science and Engineering*, vol. 691, no. 1. IOP Publishing, 2019, p. 012093.
- [4] K. W. Eastwood, P. Francis, H. Azimian, A. Swarup, T. Looi, J. M. Drake, and H. E. Naguib, "Design of a contact-aided compliant notched-tube joint for surgical manipulation in confined workspaces," *Journal of Mechanisms and Robotics*, vol. 10, no. 1, 2018.
- [5] P. A. York, P. J. Swaney, H. B. Gilbert, and R. J. Webster, "A wrist for needle-sized surgical robots," in *2015 IEEE International Conference on Robotics and Automation (ICRA)*. IEEE, 2015, pp. 1776–1781.
- [6] P. J. Swaney, P. A. York, H. B. Gilbert, J. Burgner-Kahrs, and R. J. Webster, "Design, fabrication, and testing of a needle-sized wrist for surgical instruments," *Journal of medical devices*, vol. 11, no. 1, 2017.
- [7] K. W. Eastwood, H. Azimian, B. Carrillo, T. Looi, H. E. Naguib, and J. M. Drake, "Kinetostatic design of asymmetric notch joints for surgical robots," in *2016 IEEE/RSJ International Conference on Intelligent Robots and Systems (IROS)*. IEEE, 2016, pp. 2381–2387.
- [8] T. Kato, I. Okumura, H. Kose, K. Takagi, and N. Hata, "Extended kinematic mapping of tendon-driven continuum robot for neuroendoscopy," in *2014 IEEE/RSJ International Conference on Intelligent Robots and Systems*. IEEE, 2014, pp. 1997–2002.
- [9] F. Dewaele, A. F. Kalmar, F. De Ryck, N. Lumen, L. Williams, E. Baert, H. Vereecke, J. P. Kalala Okito, C. Mabilde, B. Blanckaert, et al., "A novel design for steerable instruments based on laser-cut nitinol," *Surgical innovation*, vol. 21, no. 3, pp. 303–311, 2014.
- [10] A. Gao, R. J. Murphy, H. Liu, I. I. Iordachita, and M. Armand, "Mechanical model of dexterous continuum manipulators with compliant joints and tendon/external force interactions," *IEEE/ASME Transactions on Mechatronics*, vol. 22, no. 1, pp. 465–475, 2016.
- [11] Y. Chitalia, X. Wang, and J. P. Desai, "Design, modeling and control of a 2-dof robotic guidewire," in *2018 IEEE International Conference on Robotics and Automation (ICRA)*. IEEE, 2018, pp. 32–37.
- [12] Y. Chitalia, S. Jeong, N. Deaton, J. J. Chern, and J. P. Desai, "Design and kinematics analysis of a robotic pediatric neuroendoscope tool body," *IEEE/ASME Transactions on Mechatronics*, vol. 25, no. 2, pp. 985–995, 2020.
- [13] Z. Du, W. Yang, and W. Dong, "Kinematics modeling of a notched continuum manipulator," *Journal of Mechanisms and robotics*, vol. 7, no. 4, 2015.
- [14] D. Wei, Y. Wenlong, H. Dawei, and D. Zhijiang, "Modeling of flexible arm with triangular notches for applications in single port access abdominal surgery," in *2012 IEEE International Conference on Robotics and Biomimetics (ROBIO)*. IEEE, 2012, pp. 588–593.
- [15] S. C. Ryu, P. Renaud, R. J. Black, B. L. Daniel, and M. R. Cutkosky, "Feasibility study of an optically actuated mr-compatible active needle," in *2011 IEEE/RSJ international conference on intelligent robots and systems*. IEEE, 2011, pp. 2564–2569.
- [16] N. Lobontiu, M. Cullin, T. Petersen, J. A. Alcazar, and S. Noveanu, "Planar compliances of symmetric notch flexure hinges: The right circularly corner-filled parabolic design," *IEEE Transactions on Automation Science and Engineering*, vol. 11, no. 1, pp. 169–176, 2013.
- [17] X. Dong, M. Raffles, S. Cobos-Guzman, D. Axinte, and J. Kell, "A novel continuum robot using twin-pivot compliant joints: design, modeling, and validation," *Journal of Mechanisms and Robotics*, vol. 8, no. 2, 2016.
- [18] Y. Chitalia, S. Jeong, J. Bok, V. Nguyen, S. Melkote, J. J. Chern, and J. P. Desai, "Towards the design and development of a pediatric neuroendoscope tool," in *2019 IEEE/RSJ International Conference on Intelligent Robots and Systems (IROS)*, 2019, pp. 2998–3004.
- [19] Y. Hu, L. Zhang, W. Li, and G.-Z. Yang, "Design and fabrication of a 3-d printed metallic flexible joint for snake-like surgical robot," *IEEE Robotics and Automation Letters*, vol. 4, no. 2, pp. 1557–1563, 2019.
- [20] M. Hwang and D.-S. Kwon, "Strong continuum manipulator for flexible endoscopic surgery," *IEEE/ASME Transactions on Mechatronics*, vol. 24, no. 5, pp. 2193–2203, 2019.
- [21] J. Dearden, C. Grames, J. Orr, B. D. Jensen, S. P. Magleby, and L. L. Howell, "Cylindrical cross-axis flexural pivots," *Precision Engineering*, vol. 51, pp. 604–613, 2018.
- [22] P. Bilancia, M. Baggetta, G. Berselli, L. Bruzzone, and P. Fanghella, "Design of a bio-inspired contact-aided compliant wrist," *Robotics and Computer-Integrated Manufacturing*, vol. 67, p. 102028, 2021.
- [23] S. Awtar, A. H. Slocum, and E. Sevincer, "Characteristics of beam-based flexure modules," *Journal of Mechanical Design*, vol. 129, p. 625, 2007.
- [24] P. Bilancia, G. Berselli, S. Magleby, and L. Howell, "On the modeling of a contact-aided cross-axis flexural pivot," *Mechanism and Machine Theory*, vol. 143, p. 103618, 2020.
- [25] F. Ma and G. Chen, "Modeling large planar deflections of flexible beams in compliant mechanisms using chained beam-constraint-model," *Journal of Mechanisms and Robotics*, vol. 8, no. 2, 2016.
- [26] A. Gao, N. Liu, M. Shen, M. EMK Abdelaziz, B. Temelkurur, and G.-Z. Yang, "Laser-profiled continuum robot with integrated tension sensing for simultaneous shape and tip force estimation," *Soft Robotics*, vol. 7, no. 4, pp. 421–443, 2020.
- [27] M. D. Kutzer, S. M. Segreti, C. Y. Brown, M. Armand, R. H. Taylor, and S. C. Mears, "Design of a new cable-driven manipulator with a large open lumen: Preliminary applications in the minimally-invasive removal of osteolysis," in *2011 IEEE International Conference on Robotics and Automation*. IEEE, 2011, pp. 2913–2920.